Mon. Not. R. Astron. Soc. **000**, 1–9 (2008) Printed 8 September 2008 (MN LATEX style file v2.2)

The onset of star formation in primordial haloes

U. Maio[1⋆] B. Ciardi[1⋆], N. Yoshida[2⋆], K. Dolag[1⋆], L. Tornatore[3⋆].
[1]*Max-Planck-Institut für Astrophysik, Karl-Schwarzschild-Straße 1, D-85748 Garching b. München, Germany.*
[2]*Department of Physics, Nagoya University, Nagoya, Aichi 464-8602, Japan.*
[3]*Osservatorio astronomico di Treiste – INAF, Via Tiepolo 11, 34143 Trieste, Italy.*

September 2008

ABSTRACT
Star formation is still an unsolved problem in Astrophysics. Numerical studies of large-scale structure simulations cannot resolve the whole process and their approach is usually based on the assumption that only gas denser than a typical threshold can host and form stars.
We investigate the onset of cosmological star formation and compare different modeling running very high resolution, three-dimensional, N-body/hydrodynamic simulations including non-equilibrium, atomic and molecular chemistry, star formation prescriptions and feedback effects. We study how the primordial star formation rate changes accordingly to different gas density thresholds, cosmological parameters and initial set-ups.
We find that for mean density initial conditions low density star formation thresholds ($0.2\,h^2\,{\rm cm}^{-3}$) predict the onset at $z\sim\ 25-30$, depending on the adopted cosmology. Choosing higher density thresholds ($135\,h^2\,{\rm cm}^{-3}$) allows to follow the whole cooling process and to estimate the onset of star formation at redshifts $z\sim 12-16$. When rare, high density regions are considered the chemical evolution is much faster and the first star formation episodes show up at $z\sim 48$, or so.
Such results could have relevant implications on the formation redshift of the first cosmological objects, as inferred from direct numerical simulations, and on the reionization epoque of the Universe.

Key words: Cosmology - structure formation - simulations

1 INTRODUCTION

Understanding primordial structure formation is one of the fundamental issues of modern Astrophysics and Cosmology. There is wide agreement on the fact that the Universe is not only made of ordinary "baryonic" matter, but also of a relevant fraction of unknown "dark" matter, whose effects are only gravitational. According to recent measurements, baryonic matter would be only a small fraction of the total cosmological matter content with a present-day density parameter $\Omega_{0,b}\ =\ 0.0441$, versus $\Omega_{0,m}\ =\ 0.258$ (Hinshaw et al. 2008). As the Universe is observed to have zero curvature, i.e. to have a total density parameter $\Omega_{0,tot}\ =\ 1$, the previous data imply an additional density term $\Omega_{0,\Lambda}=\ 0.742$. This is probably related to the so-called "cosmological constant" (Einstein 1917) or, as initially suggested by Ratra & Peebles (1988), Brax & Martin (1999), Peebles & Ratra (2003), to other kinds of unknown "dark energies", whose effects on structure formation history have been firstly studied by Maio et al. (2006) via numerical simulations, and by Crociani et al. (2008) via analitycal calculations.

⋆ E-mail: maio@mpa-garching.mpg.de (UM); ciardi@mpa-garching.mpg.de (BC); nyoshida@a.phys.nagoya-u.ac.jp (NY); kdolag@mpa-garching.mpg.de (KD); tornator@oats.inaf.it (LT).

The existence of non-baryonic matter has been suggested several decades ago and structure formation models based on the growth of primordial gravitational instabilities (Peebles 1974) were developed since the early works by Gunn & Gott (1972).
Hydrodynamical simulation codes (the first dating back to Evrard 1988) have been a powerful mean of study, but computational limitations have always requested plausible sub-grid models to take into account star formation events (e.g. Cen & Ostriker 1992; Katz et al. 1996; Springel & Hernquist 2003).
The basic idea of such investigations relies on the converging gas in-fall into dark matter potential wells: during this process gas is shock heated and subsequently cools down via energy level transitions. The typical time-scales involved in the process are the free-fall time, t_{ff}, and the cooling time, t_{cool}. Gas condensation is supposed to take place only if $t_{cool} < t_{ff}$.
The free-fall time is defined as

$$t_{ff} = \sqrt{\frac{3\pi}{32G\rho}} \qquad (1)$$

where G is the universal gravitational constant and ρ the density of the medium; the numeric factor $(3\pi/32)^{1/2}$ holds rigorously for spherical symmetry only. The cooling time is defined as

$$t_{cool} = \frac{3}{2}\frac{nk_BT}{\mathcal{L}(T,n_i)} \qquad (2)$$

where n is the number density of the gas, k_B the Boltzmann constant, T the temperature and $\mathcal{L}(T, n_i)$ the cooling function (energy emitted per unit time and volume) dependent both on temperature and number densities, n_i, of the species constituting the gas. In the usually adopted low-density limit[1], for two-body interactions, between e.g. particle x and particle y, $\mathcal{L}$ can be written as

$$\mathcal{L}(T, n_x, n_y) = \Lambda(T) n_x n_y \quad (3)$$

with $\Lambda(T)$ a quanto-mechanic function dependent on the temperature and the number densities of the species considered, n_x and n_y. At $T \geqslant 10^4$ K, the cooling is dominated by collisions of hydrogen atoms, which is the most abundant species in nature – about 93% in number fraction – and $\mathcal{L}$ scales approximatively as n_H^2 (we indicate with n_H the hydrogen number density).

The physical conditions in which the first structures form are characterized by a primordial chemical composition: mostly hydrogen, deuterium, helium and some derived molecules, like H_2 and HD.

The primordial sites where the first stars form are thought to be small dark matter haloes with masses $\sim 10^6\,\mathrm{M}_\odot$ – as expected from predictions based on self-similar gravitational condensation and chemical evolution (Press & Schechter 1974; Tegmark et al. 1997; Sheth & Tormen 1999; Jenkins et al. 2001; Haiman & Bryan 2006, etc.) – and virial temperatures $T_{vir} \lesssim 10^4$ K. Once they are born, they illuminate the Universe for the first time and mark the end of the "dark ages". The radiation propagates around the individual sources and the impact on the subsequent structure formation (Ricotti et al. 2002a,b, 2008) can be very significant leaving imprints via a number of feedback effects (see Ciardi & Ferrara 2005, for a review).

The low values of virialization temperatures of primordial haloes are enough neither to excite nor to ionize hydrogen and the lack of any metals means that the gas can cool and eventually form objects only via molecular transitions (Saslaw & Zipoy 1967; Peebles & Dicke 1968; Hollenbach & McKee 1979; Abel et al. 1997; Galli & Palla 1998; Maio et al. 2007, for a detailed study on the efficiency of cooling in different regimes). In fact, they have rotational energy separations with excitation temperatures below 10^4 K, and therefore it is possible to collisionally populate their higher levels with consequent emission of radiation and resulting gas cooling. Of course, as the molecular energy separations are lower than the atomic ones, cooling will be slower, but still capable to bring the temperature down to $\lesssim 10^2$ K (Yoshida et al. 2003; Omukai & Palla 2003; Yoshida et al. 2006; Gao et al. 2007).

In order to follow the whole process of structure and star formation in numerical simulations, one should implement the entire set of chemical reactions and hydrodynamical equations and from those calculate the abundance evolution and the corresponding cooling term. In practice, to perform such computations is very expensive and time consuming and it becomes extremely challenging to follow the formation of structures from the initial gas in-fall into the dark matter potential wells to the final birth of stars. Nevertheless, efforts are being made in this direction (e.g. Abel et al. 2000, 2002; Bromm & Larson 2004; Yoshida et al. 2007; Whalen et al. 2008).

[1] This approximation is appropriate as, according to the classical spherical "top-hat" model, a virialized object has a total mass density of $18\pi^2$ times the critical density, which corresponds, on average, to a total number density of $\sim 2\,h^2\,\mathrm{cm}^{-3}$ at $z \sim 15$, for a WMAP5 cosmology and a mean molecular weight $\mu \simeq 1$. The transition to a high density statistical equilibrium regime happens at critical number densities of $\sim 10^4\,\mathrm{cm}^{-3}$.

For this reason, more practical, even if sometimes coarse, approximations are adopted. In brief, star formation relies on semi-empirical and numerical recipes based on some criteria to convert gas into stars and get the star formation rate, carefully normalized to fit observational data at the present day. The standard method used is to assume that once the gas has reached a given density threshold it automatically forms stars (e.g. Cen & Ostriker 1992; Katz et al. 1996; Springel & Hernquist 2003), regardless of the time between the moment when the threshold is reached and the effective run-away collapse which is typically at densities $\sim 10^2 - 10^4\,\mathrm{cm}^{-3}$. While this might be a reasonable approximation at low redshift, at high redshift this interval of time occupies a large fraction of the Hubble time and thus this assumption can induce large artificial off-sets on the onset of star formation and influence the evolution of the star formation rate. Thus, extrapolations to high redshifts of the low density thresholds (few $0.1\ \mathrm{cm}^{-3}$) used to model the star formation rate in the low redshift Universe, might be not always justifiable. For this reason, high redshift applications require larger resolutions and a higher density threshold.

In this paper we discuss the importance of the choice of the density threshold in simulations of early structure formation and first stars. We propose a criterion to choose such threshold (section 2) and discuss some test cases and results based on high resolution simulations (section 3 and 4).

2 THRESHOLD FOR STAR FORMATION

According to the usual scenario of structure formation, the Jeans mass (Jeans 1902) is the discriminant quantity which allows to distinguish collapsing from non-collapsing objects, under gravitational instability. Its expression for a perfect, isothermal, gas is:

$$M_J = \frac{\pi}{6}\left(\frac{k_B T}{\mu m_H G}\right)^{3/2} \rho^{-1/2} \quad (4)$$

where m_H is the mass of the hydrogen atom and T and ρ the temperature and density of the gas, respectively. At very high redshift ($z \sim 30 - 20$), typical haloes have masses of $\sim 10^5 - 10^6\,\mathrm{M}_\odot$ which can grow up to $\sim 10^8 - 10^9\,\mathrm{M}_\odot$ at $z \sim 10$.

As mentioned in the introduction, typically in numerical simulations the density threshold for star formation is fixed to some constant value, irrespectively of the resolution of the simulation. It would be desirable instead to have a star formation criterion that allows to reach scales that resolve the Jeans mass.

If M_{res} is the gas mass resolution of a given simulation, we can require that:

$$M_J = N M_{res} \quad (5)$$

with $N > 1$ and impose the critical threshold to be

$$\rho_{th} = \frac{\pi^2}{36 N^2 M_{res}^2}\left(\frac{k_B T}{\mu m_H G}\right)^3 \quad (6)$$

$$\simeq \frac{1.31 \cdot 10^{-13}}{N^2}\left(\frac{M_{res}}{\mathrm{M}_\odot}\right)^{-2}\left(\frac{T}{10^3\ \mathrm{K}}\right)^3\left(\frac{1}{\mu}\right)^3\ [\mathrm{g\,cm}^{-3}]. \quad (7)$$

For $M_{res} = 10^2\ \mathrm{M}_\odot$, $T = 10^3$ K, $\mu = 1$ and using $N = 10^2$ gas particles, one has $\rho_{th} \sim 10^{-21}\,\mathrm{g\,cm}^{-3}$, corresponding to a number density of some $10^2\,\mathrm{cm}^{-3}$. Typically, the commonly adopted density thresholds are of the order of $\sim 10^{-1}\,\mathrm{cm}^{-3}$.

Table 1. Parameters adopted for the simulations. The columns (from left to right) refer to: name of the run, number of particles used, gas particle mass, dark matter particle mass, Ω_{0M}, $\Omega_{0\Lambda}$, Ω_{0b}, h, σ_8, spectral index, star formation density threshold.

Model	number of gas/dm particles	M_{gas} $[\mathrm{M}_\odot/h]$	M_{dm} $[\mathrm{M}_\odot/h]$	Ω_{0M}	$\Omega_{0\Lambda}$	Ω_{0b}	h	σ_8	n	SF threshold $[h^2\mathrm{cm}^{-3}]$
wmap5-ht	2×32768000	128	621	0.258	0.742	0.0441	0.72	0.8	0.96	135
wmap5-lt	2×32768000	128	621	0.258	0.742	0.0441	0.72	0.8	0.96	0.2
std-ht	2×32768000	116	755	0.300	0.700	0.0400	0.70	0.9	1.00	135
std-lt	2×32768000	116	755	0.300	0.700	0.0400	0.70	0.9	1.00	0.2
zoom-std-ht	2×41226712	3.9	25.6	0.300	0.700	0.0400	0.70	0.9	1.00	135

To investigate the effects of different choices of star formation threshold on structure formation at high redshift, we implement the above recipe in numerical simulations. In the following we describe the simulations performed and show the results obtained.

3 SIMULATION SET-UP

In order to study the effect of different threshold prescriptions on the onset of star formation we run very high resolution, three-dimensional, hydrodynamic simulations including non-equilibrium atomic and molecular chemistry, star formation and wind feedback. We use the code Gadget-2 (Springel 2005) in the modified version including stellar evolution and metal pollution (Tornatore et al. 2007), with the implementation of primordial molecular chemistry (following the evolution of e^-, H, H^+, He, He^+, He^{++}, H_2, H_2^+, H^-, D, D^+, HD, HeH^+) and fine structure metal transition cooling (O, C^+, Si^+, Fe^+) at temperatures lower than 10^4 K (Maio et al. 2007, 2008).
The simulations have a comoving box size of $L = 1\,\mathrm{Mpc}$ and sample the cosmological medium with a uniform realization of 320^3 particles for both gas and dark matter species (for a total number of 2×320^3). The initial conditions (set at redshift $z = 100$) are generated using N-GenIC by a fast Fourier transform grid with $N_{mesh} = 320$ meshes and a maximum wave-number (Nyquist frequency)

$$k_{Nyquist} = \frac{2\pi N_{mesh}}{2L} \simeq 1\ \mathrm{kpc}^{-1}$$

(i.e. a minimum wavelength of $2L/N_{mesh} \simeq 6.25$ kpc) so that, for each wave-number, $\|\mathbf{k}\| < k_{Nyquist}$.
For our purposes we consider two different sets of cosmological parameters:

- *standard model*: $\Omega_{0,m} = 0.3$, $\Omega_{0,\Lambda} = 0.7$, $\Omega_{0,b} = 0.04$, $h = 0.7$, $\sigma_8 = 0.9$ and $n = 1$, where the symbols have the usual meaning. The corresponding dark matter and gas particle masses are $\sim 755\,\mathrm{M}_\odot/h$ and $\sim 116\,\mathrm{M}_\odot/h$, respectively.
- *WMAP5 model*: recent data from 5-year WMAP (WMAP5) satellite (Hinshaw et al. 2008) suggest: $\Omega_{0,m} = 0.258$, $\Omega_{0,\Lambda} = 0.742$, $\Omega_{0,b} = 0.0441$, $h = 0.72$, $\sigma_8 = 0.796$ and $n = 0.96$. In this case, the corresponding dark matter and gas particle masses are $\sim 621\,\mathrm{M}_\odot/h$ and $\sim 128\,\mathrm{M}_\odot/h$, respectively.

Following the discussion in the previous sections, we also consider two different models for the star formation density threshold:

- a *low density* threshold of $0.2\,h^2\mathrm{cm}^{-3}$ (physical), as adopted in Gadget code and widely used in the literature (for example Springel & Hernquist 2003; Tornatore et al. 2007; Pawlik et al. 2008);
- a *high density* threshold of $135\,h^2\mathrm{cm}^{-3}$ (physical), as computed from the previous steps (6) and (7). This value is adequate to follow atomic processes even in small $\sim 10^5\,\mathrm{M}_\odot$ haloes at $z \sim 20$. Moreover, typically this threshold falls in density regimes when cooling dominates over heating and thus allows to properly resolve gas condensation down to the bottom of the cooling branch.

A summary with all the features of the simulations is given in table 1. We denote with the labels "std" and "wmap5" the runs with standard and WMAP5 cosmology, respectively; with "lt" and "ht" the runs with low and high density threshold, respectively.

Finally, to investigate primordial star formation events in local high density regions, we perform a very high resolution numerical simulation of a rare high sigma peak with comoving radius $\sim 140\,\mathrm{kpc}/h$. Such region is selected using the zoomed initial condition technique on a $\sim 10^9\,\mathrm{M}_\odot$ halo formed in a dark matter only simulation (Gao et al. 2007)[2]. We split each particle in gas and dark matter component, according to the standard model parameters. The resulting gas particle mass is $\sim 4\,\mathrm{M}_\odot/h$ while dark matter particles have a mass of $\sim 26\,\mathrm{M}_\odot/h$ (in table 1 this simulation is labelled with "zoom-std-ht").

4 RESULTS

In this section we show results from simulations with the previous sets of parameters. We discuss first the mean region of the Universe (section 4.1) and then the high density region (section 4.2).

4.1 Mean region simulation

Our reference run is the wmap5-ht model with initial composition given by the values quoted in Galli & Palla (1998)[3] at $z = 100$. We show some evolutionary stages in Figure 1 (upper set of panels). In the maps, the first column refers to temperature, the second to gas density and the third to molecular fraction at $z = 30.16$ and $z = 12.17$, respectively. The creation of new molecules is evident, together with the related growth of structure. More specifically, as time passes, one can see the heating undergone by the gas in dense regions, due to structure formation shocks. The temperature increases from few hundreds Kelvin in the low density regions, to

[2] We use the "R4" initial conditions presented there.
[3] We assume a primordial neutral plasma with residual electron and H^+ fractions $x_{e^-} \simeq x_{H^+} \simeq 4 \cdot 10^{-4}$, H_2 fraction $x_{H_2} = 10^{-6}$, H_2^+ fraction $x_{H_2^+} = 3 \cdot 10^{-21}$, D fraction $x_D = 3.5 \cdot 10^{-5}$, HD fraction $x_{HD} = 7 \cdot 10^{-10}$, D^+ fraction $x_{D^+} = 4 \cdot 10^{-9}$, HeH^+ fraction $x_{HeH^+} = 10^{-14}$.

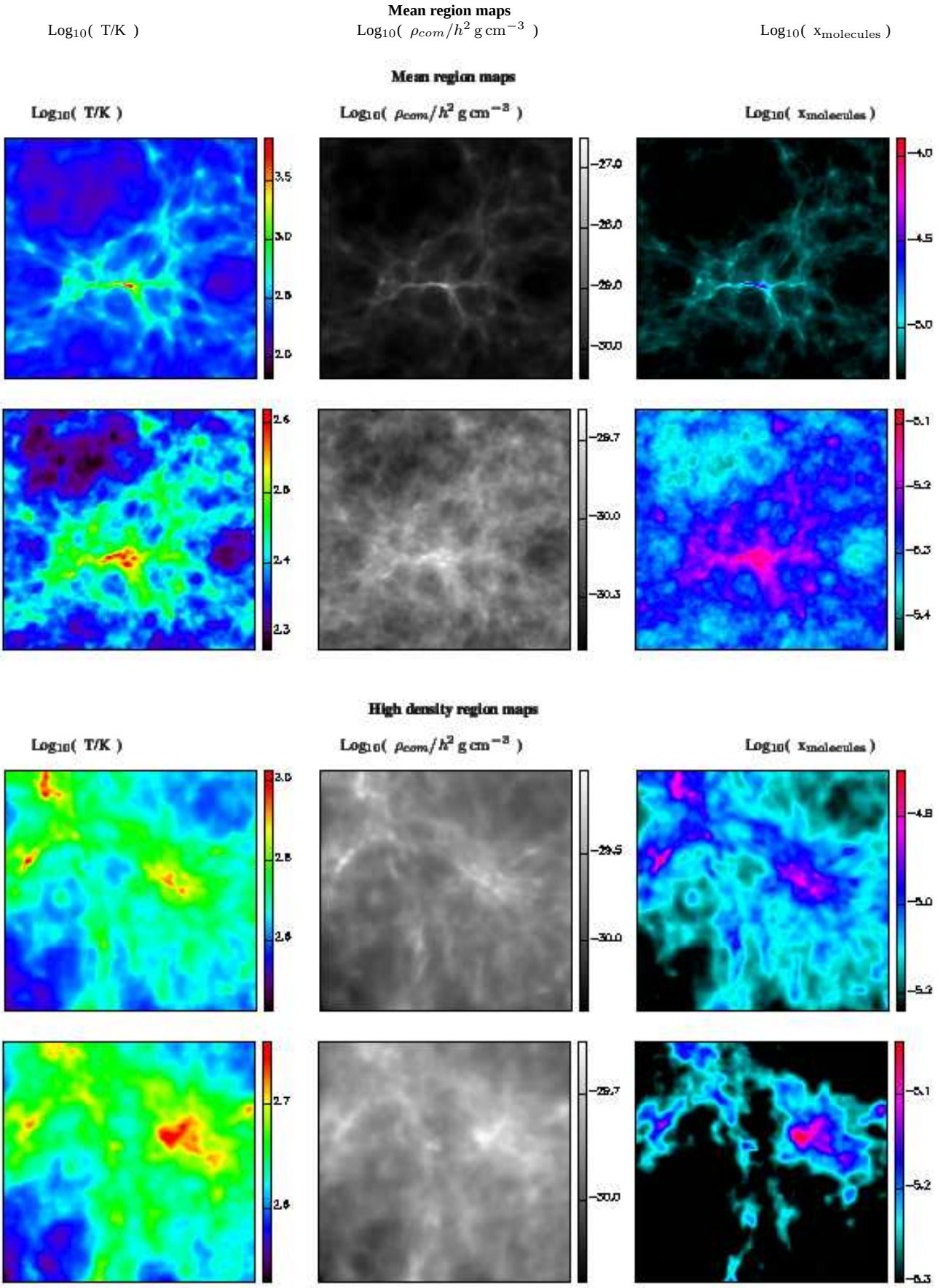

Figure 1. First, second and third column are respectively temperature, density and molecule maps. The first two rows refer to the mean region simulation at redshift 12.17 and 30.16, from top to bottom. The box size is 1 Mpc comoving. The last two rows refer to the high density region at redshift 50 and 70 respectively, from top to bottom. The region size is $\sim 140\,\mathrm{kpc}/h$ comoving. The different quantities are smoothed on a 276 pixel side grid.

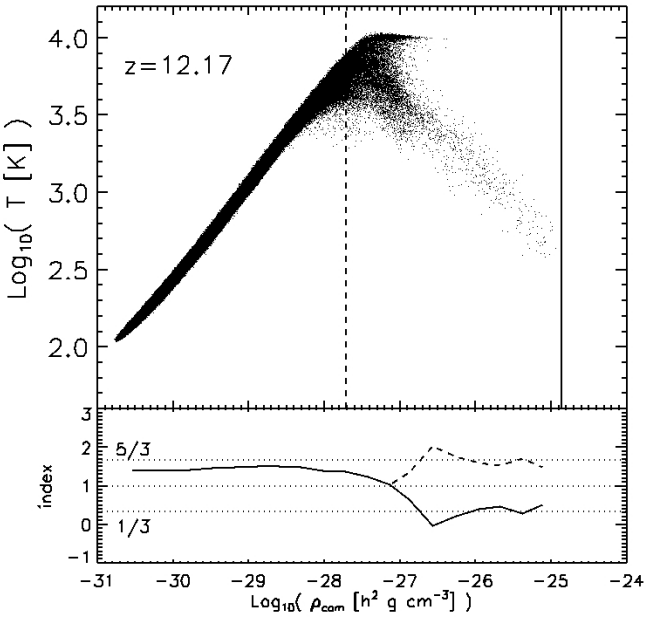

Figure 2. *Upper panel*: phase diagram at redshift $z = 12.17$ (soon before the onset of star formation) for the wmap5-ht simulation. The vertical straight lines are drawn in correspondence of a low physical critical density threshold of $0.2\ h^2\mathrm{cm}^{-3}$ (dashed line) and a higher physical critical density threshold of $135\ h^2\mathrm{cm}^{-3}$ (solid line). *Lower panel*: average effective index computed over the whole range of densities. The three horizontal dotted lines are drawn in correspondence of the values 5/3, 1 and 1/3, respectively, from top to bottom. The solid line refers to α and the dashed line to γ (see text for the definitions).

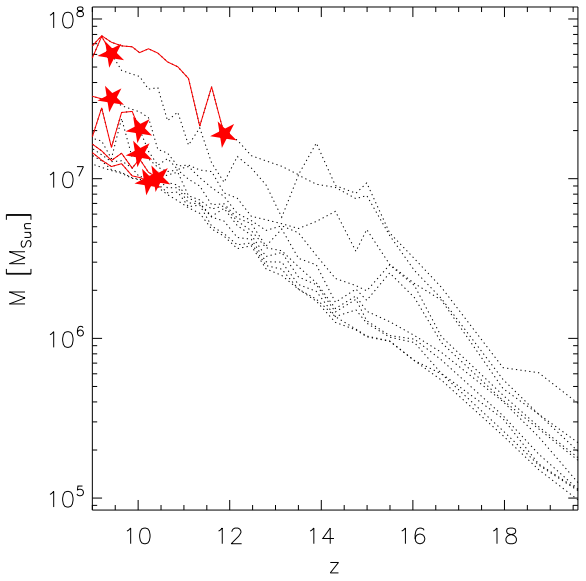

Figure 3. Evolution of the ten most massive haloes in the wmap5-ht cosmological simulation (dotted lines). The redshift at which the first star forms in each halo is indicated by the filled star symbols. After that, star formation continues along the solid lines.

$\sim 10^4$ K in the denser regions. In the meantime, also the molecular fraction evolves accordingly up to values larger than 10^{-4}. Soon after, the production of molecules increases rapidly (up to $\sim 10^{-2}$) enhancing the star formation process, which, for this simulation, starts at $z \sim 12$.

In Figure 2, we show the phase diagram (comoving density versus temperature) at redshift $z \sim 12$, i.e. just before the onset of star formation. The low density gas shock heated by the collapse of the first primordial haloes is seen on the left side of the panel. Starting from values of the temperature of $\sim 10^2$ K, the gas is progressively heated to $\sim 10^4$ K and moves along the increasing branch. At this stage, collisions become more frequent because of the higher temperature. The upper energy levels of particles get excited and the subsequent de-excitation is accompanied by emission of radiation. The latter effect is negligible at low densities, because the collisions are rare and the fraction of energy converted into radiation is small. When the density increases, the cooling becomes comparable to the heating and an isothermal regime with no significant net change in the temperature is reached. This is visible at the tip of the phase diagram (and in the behavior of the effective index, as discussed below), at $T \sim 10^4$ K, where the cooling is dominated essentially by atomic Lyα transitions and accompanied by fragmentation, as the Jeans mass becomes proportional to $\rho^{-1/2}$.
At higher densities, radiative losses overtake heating and induce a fast cooling phase (dominated by molecules, mostly H_2) which is approximatively adiabatic. This eventually halts the fragmentation process freezing the minimum mass of gas clouds and enhancing star formation.
The solid vertical line corresponds to the physical high density star formation threshold ($135\ h^2\ \mathrm{cm}^{-3}$) and, for comparison, we plot also the dashed line for a physical number density of $0.2\ h^2\ \mathrm{cm}^{-3}$. We stress the fact that by adopting a low density threshold for star formation one completely misses the isothermal and adiabatic part of the cooling diagram, and thus a correct modeling of the cooling regions within the simulations. This can affect the onset of star formation, particularly at high redshift, when the time needed for the gas to evolve from the low density threshold to the high density threshold ($\sim 2 \cdot 10^8$ yr) can be a substantial fraction of the Hubble time ($\sim 4 \cdot 10^8$ yr at $z \sim 12$). Note that the time elapsed between the attainment of the isothermal peak in the phase diagram and the end of the adiabatic branch is $\sim 6 \cdot 10^7$ yr. The evolution that follows the end of the adiabatic branch is characterized by the formation of a dense core and gas accretion onto it in free-fall time-scales (Yoshida et al. 2006). This phase is very fast ($\sim 10^6 - 10^7$ yr) and rapidly brings central densities up to $\sim 10^{16}\ \mathrm{cm}^{-3}$.
As a consequence of the above considerations, the onset of star formation can happen much earlier in models with a low density threshold (as we will show in the following). This problem is less sever at lower redshift, when the Hubble time becomes of the order of several Gyr.

In addition, density and temperature behavior can be described with an effective index dependent on the physical conditions of the gas regime considered. In the lower panel of Figure 2 we plot the effective index as a function of density. The solid line refers to the value $\alpha \equiv 1 + (\mathrm{d}T/T)/(\mathrm{d}\rho/\rho)$, which takes into account changes in the sign of the temperature derivative distinguishing the heating regime ($\alpha > 1$) from the cooling regime ($\alpha < 1$). The dashed line refers to $\gamma \equiv 1 + |(\mathrm{d}T/T)/(\mathrm{d}\rho/\rho)|$, so that γ is always $\geqslant 1$. The three dotted horizontal straight lines are drawn in correspondence of the values $5/3$, 1 and $1/3$, from top to bottom.
In correspondence of the isothermal peak in the $T - \rho$ plane,

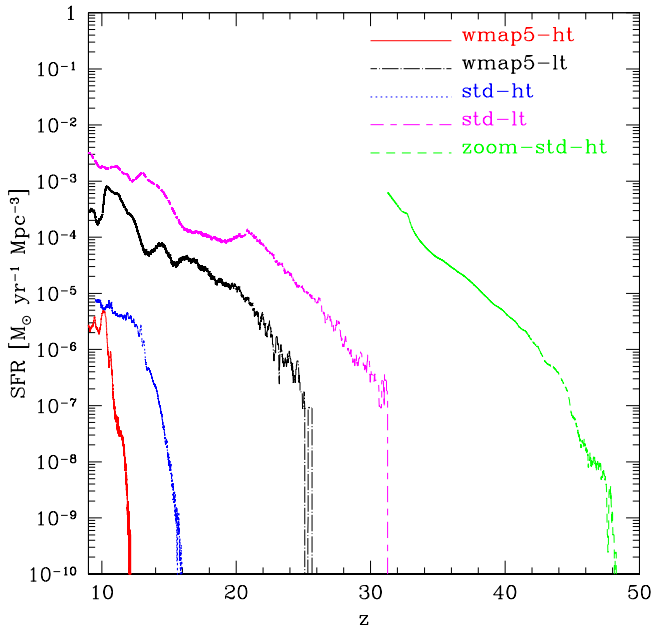

Figure 4. Star formation rate as a function of redshift for the different models, from left to right: WMAP5 cosmology and high density threshold (solid red line), standard cosmology and high density threshold (dotted blue line), WMAP5 cosmology and low density threshold (dot-dashed black line), standard cosmology and low density threshold (long-dashed-short-dashed magenta line). The green short-dashed line refers to the simulation of the high density region with standard parameters and high density threshold.

$\alpha = \gamma = 1$, which marks the transition from the heating to the cooling regime. According to the Jeans theory, at this stage we expect the gas run-away collapse to set in until the following cooling regime is reached, when γ oscillates around the adiabatic value and the process is halted. Indeed, gas condensation and accretion act against further cooling, heating up the whole system. When central temperatures raise to $\sim 10^7$ K, the proton-proton chain becomes efficient and sustains a H nuclear burning stellar core (Yoshida et al. 2006, 2007).

In Figure 3, we plot the evolution of the ten most massive haloes found in the simulation. We also show the redshift when stars are produces (filled star symbols) in each object. The haloes are found using a friend-of-friend algorithm with a linking length equal to 20% the mean inter-particle separation. Typical halo masses at redshift $z \sim 12$, when star formation starts, are of the order of $10^7\,\mathrm{M}_\odot$ and reach densities of $\sim 10^2\,\mathrm{cm}^{-3}$.

As a comparison, we have run the same simulation using standard cosmological parameters (std-ht run). In this case we expect a faster evolution, with an earlier structure formation. In fact, the first star formation events are detected already at redshift $z \sim 16$ in haloes with masses $\sim 10^7\,\mathrm{M}_\odot$.

This can be clearly seen in Figure 4, where we plot the star formation rate as a function of redshift for the different simulations. In order to compute the star formation rate, we adopt the implementation described by Springel & Hernquist (2003).
The onset of star formation in the wmap5-ht model (red solid line) is postponed in comparison to the std-ht model (blue dotted line). Thus, at such high redshifts, also small changes in the cosmology can be significant for the onset of star formation. This is easily understood in terms of spectral parameters: the standard cosmology has higher index and higher normalization, therefore assigns more power to all scales, with respect to WMAP5 values and structure formation happens much earlier.
The effect of a different choice of the density threshold makes an even larger difference in the onset of star formation. In Figure 4 the star formation rate corresponding to the wmap5-lt (black dot-dashed line) and std-lt (magenta short-long-dashed line) shows that star formation starts at $z \sim 25$ and 31, respectively. The big difference in star formation between low and high density threshold models is due to the fact that in the former, the gas reaches the critical density much earlier. So, the redshift difference in the onset corresponds to the time that the gas needs to arrive from the low to the high density threshold (see Figure 2).
As already mentioned, the low density threshold model is very commonly used both in numerical and semi-analytical works, because it does not require following molecular chemistry (as the threshold is lower than the typical densities at which molecules become efficient coolants) and therefore it is easier to implement and allows for faster simulations. Nonetheless, it can compromise the whole picture if the results are extrapolated to high redshift, when molecules are the main coolants and the time delay between the attainment of the low density threshold and the bottom of the cooling branch occupies a significant fraction of the Hubble time.

4.2 High density region simulation

In this section we show the results relative to the high density region described in section 3 and initialized at redshift $z = 399$.
In this case, the physical number densities at the beginning of the simulation are in the range $\sim 0.5 - 50\,h^2\,\mathrm{cm}^{-3}$ (at $z \sim 200$), with an average of $\sim 4\,h^2\,\mathrm{cm}^{-3}$, higher than the typical value adopted for the low density threshold for star formation. So, the conventional low-density model results in unreasonable star formation at $z \sim 200$.
Therefore, we run a simulation only with a high density threshold. For the sake of comparison, we still use the value of $135\,h^2\,\mathrm{cm}^{-3}$, although rigorously, following (6) and (7), one should adopt a value $\sim 9 \cdot 10^4\,h^2\,\mathrm{cm}^{-3}$ for a 3.9 $\mathrm{M}_\odot/h$ gas particle mass. Nonetheless, we have checked that this choice does not affect our conclusions, as the threshold is already beyond the isothermal peak, in the fast cooling regime, where the time-scales are extremely short ($\sim 10^6$ yr).
All the initial abundances are set according to the values suggested by Galli & Palla (1998)[4].
The simulation maps are shown in Figure 1 (bottom set of panels). As for the mean density regions, the columns, from left to right, refer to temperature, density and molecular fraction at redshift z=50 and 70, from top to bottom. We highlight that, as expected, structure formation happens much earlier compared to the case of a region at mean density. Molecular abundances of $\sim 10^{-5}$ are reached faster than the corresponding mean density case, where such fraction is found only at $z \lesssim 30$. Accordingly, values of

[4] The initial abundances (at $z = 399$) are consistent with a primordial neutral plasma having residual electron and H^+ fractions of $x_{e^-} \simeq x_{H^+} = 10^{-3}$, H_2 fraction $x_{H_2} = 10^{-10}$, H_2^+ fraction $x_{H_2^+} = 3 \cdot 10^{-15}$, D fraction $x_D = 3 \cdot 10^{-5}$, D^+ fraction $x_{D^+} = 3 \cdot 10^{-8}$, HD fraction $x_{HD} = 10^{-14}$, HeH^+ fraction $x_{HeH^+} = 5.6 \cdot 10^{-18}$

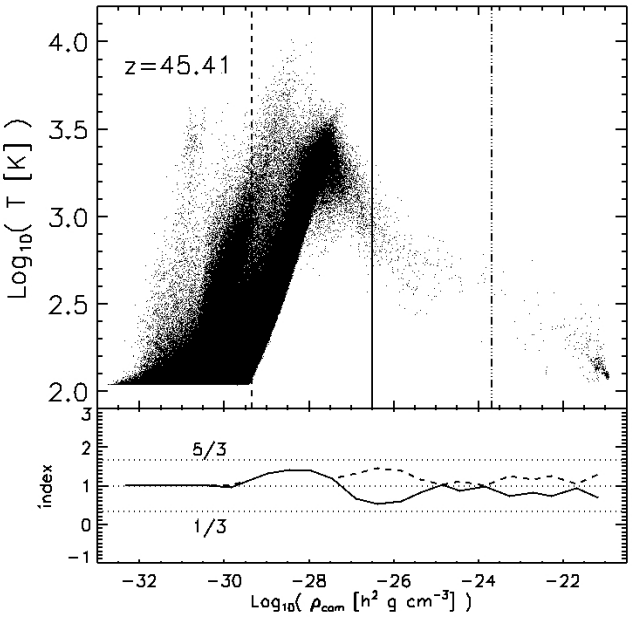

Figure 5. *Upper panel*: phase diagram at redshift $z = 45.41$ for the high density region simulation for a purely non-equilibrium chemistry run (i.e. without star formation). The vertical straight lines are drawn in correspondence of a physical critical density threshold of $0.2\,h^2\mathrm{cm}^{-3}$ (dashed line), $135\,h^2\mathrm{cm}^{-3}$ (solid line) and $8.9\cdot10^4\,h^2\mathrm{cm}^{-3}$ (dot-dashed line). *Lower panel*: average effective index computed over the whole range of densities. The three horizontal dotted lines are drawn in correspondence of the values 5/3, 1 and 1/3, respectively, from top to bottom. The solid line refers to α and the dashed line to γ (see text for the definitions).

$\sim 10^{-4}$ are already reached at $z \sim 40$, rather than $z \sim 20$, respectively.

In Figure 5, we show the phase diagram and the effective index as a function of the comoving gas density at redshift $z \simeq 45$ and we over-plot different critical densities as straight vertical lines as reference: dashed, solid and dot-dashed correspond respectively to a physical critical density threshold of $0.2\,h^2\mathrm{cm}^{-3}$, $135\,h^2\mathrm{cm}^{-3}$ and $\sim 9\cdot10^4\,h^2\mathrm{cm}^{-3}$. While the first two are the same used for the mean density region simulation, the last one corresponds to the value obtained using equations (6) and (7). To emphasize the different characteristics of the phase diagram compared to the one obtained for the mean density region, we plot also the particles that lay above the density threshold in a purely non-equilibrium chemistry run (i.e. without star formation).
The isothermal peak is reached already at redshift $z \sim 50$. Differently from the mean density simulation, the gas does not spend time on the isothermal plateau, but cools very rapidly (in less than $7\cdot10^6$ yr) from $\sim 10^{3.5}$ K to $\sim 10^2$ K and condenses into comoving densities of $\rho_{com} \sim 10^{-21}\,h^2\,\mathrm{g/cm}^3$. The rapidity of these events is reflected in the lack of particles in the intermediate stages of the cooling branch.
As before, we also plot the effective gas index in the lower panel. The usual initial shock-heating behavior and the following adiabatic cooling is recovered up to much higher densities. At the bottom of the cooling branch we find values of γ oscillating around 5/3 and 1. As the last stages are quite fast, the low number of particles present introduces some statistical noise in the plot.

With our choice of the threshold, star formation sets in at $z \sim 48$ (see Figure 4). As the additional time needed to reach the highest densities at the bottom of the cooling branch is extremely short ($\sim 10^6$ yr), such choice assures that the onset of star formation is correctly estimated. As there is no obvious, standard way of quantifying the star formation rate in these simulations, we do it dividing the stellar mass formed at each time-step by the volume of the gas contained in the high density region (a sphere of about $140\,\mathrm{kpc}/h$ radius).
On the other hand, the low density model is not helpful in the present case and in any other condition when the initial gas density is significantly above the mean density. Indeed, its mis-use would unavoidably lead to unphysical results.

5 DISCUSSION AND CONCLUSIONS

We have studied the effect of different choices of the density threshold for the creation of stellar particles on the onset of star formation in numerical SPH simulations (see Maio et al. 2007; Tornatore et al. 2007, for technical details). We have run simulations using initial conditions appropriate for both a region of the universe with mean density and, using the zoom technique, a high density peak region.

The basic process which leads to star formation, i.e. gas shock heated up to some $10^3 - 10^4$ K by in-fall into dark matter haloes followed by radiative losses due mainly to molecular collisional excitations, is common to both scenarios. The main difference is associated to the global dynamics and time-scales of the process. In fact, following the rare high sigma peak we see that, because of the higher densities, chemical reactions are faster and much more efficient with respect to the simulations with mean density initial conditions. Therefore, the molecular fraction increases more rapidly, reaching a number fraction of $\sim 10^{-4}$ already at $z \sim 40$ (compared to $z \sim 20$, for the corresponding mean density case). Such values are enough to make collisional cooling dominant over heating and to induce star formation episodes.

Density and temperature behavior can be described with an effective index dependent on the physical conditions of the gas considered. Roughly, it is isothermal during the transition from the heating to the cooling regime, then it turns to be fully adiabatic (see the effective index computed in the lower panel of Figure 2) until the bottom of the cooling branch is reached and the isothermality is recovered, as gas condensation and accretion act against further cooling, heating up the system. When central temperatures raise to $\sim 10^7$ K, the proton-proton chain becomes efficient and sustains a H nuclear burning stellar core (Yoshida et al. 2006, 2007).
More quantitatively, when cooling is dominated by H_2, the cooling time (2) can be approximated as

$$t_{cool} \simeq \frac{3}{2}\frac{k_B T}{\Lambda_{\mathrm{H}_2}(T)\; x_{\mathrm{H}_2} n_{\mathrm{H}}} \qquad (8)$$

where x_{H_2} is the H_2 number fraction, $\Lambda_{\mathrm{H}_2}(T)$ is the H_2 cooling function at temperature T and the other symbols have the usual meaning.
For gas at the beginning of the cooling branch, $T \sim 10^{3.5}$ K and $x_{\mathrm{H}_2} \sim 10^{-4}$, which gives $t_{cool} \sim 7\cdot\,10^6\,n_{\mathrm{H}}^{-1}$ yr (n_{H} in cm^{-3}). In the mean density case (see phase diagram in Fig. 2),

$n_{\rm H} \simeq 0.3\,{\rm cm}^{-3}$, while in the high density region (see phase diagram in Fig. 5), $n_{\rm H} \simeq 6\,{\rm cm}^{-3}$. This translates into a characteristic cooling time of $\sim 2 \cdot 10^7$ yr for the former case and $\sim 10^6$ yr for the latter. Such rough estimates show the relevance of following the full cooling branch when simulating star formation at high redshift in regions of mean density, because the characteristic cooling time occupies a substantial fraction of the Hubble time. This problem is less severe for simulations of high density peaks, in which the time-scales are much shorter.

For this reason it is important to use a high density threshold for star formation, rather than imposing star formation even before the isothermal peak is reached. This in fact could result in an artificially high redshift for the onset of star formation. For the test cases presented in this paper, the value adopted for the high density threshold is $135\,h^2{\rm cm}^{-3}$, well beyond the isothermal peak of the gas. This allows to have a correct estimate of the relevant time-scales, as the gas spends most of the time in the isothermal phase. In addition, following the evolution of the gas to higher densities allows a better resolution of, e.g., the morphology and disk galaxy structure (Saitoh et al. 2008), the clumpiness of the gas (see Appendix A) and the features of the interstellar (ISM) or intergalactic (IGM) medium.
It is worth noticing that the mean density region, because of its small dimension, lacks of massive haloes. In larger simulations, we expect to find more rare, high sigma peaks, which can grow faster and host star formation in $\sim 10^5 - 10^6\,{\rm M}_\odot$ haloes.

In summary, in the present work we have performed high resolution, three-dimensional, N-body/SPH simulations including non-equilibrium atomic and molecular chemistry, star formation prescriptions and feedback effects to investigate the onset of primordial star formation. We have studied how the primordial star formation rate changes according to different gas density threshold, different cosmological parameters and different simulation set-ups. Our findings are summarized in the following.

- The typical low density thresholds (below $\sim 1\,{\rm cm}^{-3}$) are inadequate to describe star formation episodes in mean regions of the universe at high redshift. To correctly estimate the onset of star formation high density thresholds are necessary.
- In rare, high density peaks, the density can be higher than the usual low density thresholds already since very early times, therefore such prescription are not physically meaningful. Density thresholds lying beyond the isothermal peak (several particles per cm^3, in our case) are still required, but given the faster evolution in the phase diagram of the cooling particles in dense environments, the exact value of the threshold is not crucial, as long as it is larger than $\sim 10^2\,{\rm cm}^{-3}$ (physical).
- Different values of the threshold and the cosmological parameters can produce very different epochs of the onset of star formation: with a low density threshold ($0.2\,h^2\,{\rm cm}^{-3}$) star formation stars at $z \sim 25 - 30$ (depending on the cosmology), while high density threshold models ($135\,h^2\,{\rm cm}^{-3}$) predict a much later onset, $z \sim 12 - 16$ (depending on the cosmology).
- Performing primordial, rare, high density region simulations within the high density threshold model, we find that the local star formation can set in as early as $z \sim 48$. Low density threshold models produce unreasonable results.

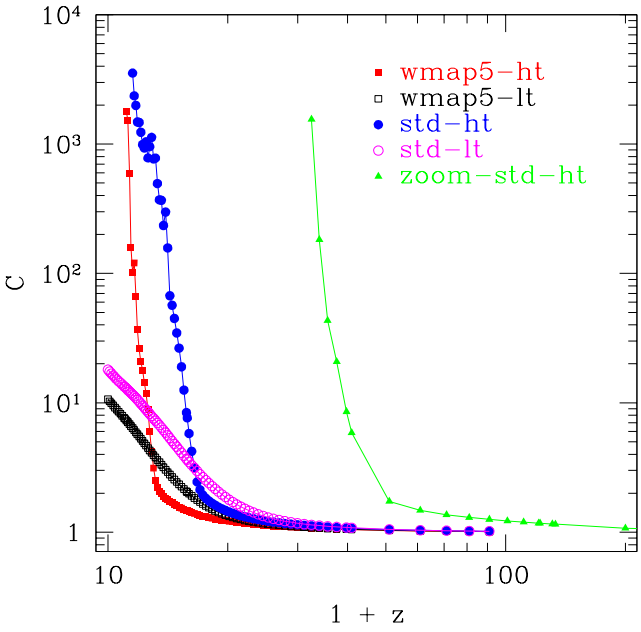

Figure A1. Global clumping factor for the different simulations as a function of redshift.

ACKNOWLEDGMENTS

We acknowledge useful discussions with Massimo Ricotti, Volker Springel, Romain Teyssier and John Wise.
The simulations were performed using the machines of the Max Planck Society computing center, Garching (Rechenzentrum-Garching) and of the Max-Planck-Institut für Astrophysik.
For the bibliografic research we have made use of the tools offered by the NASA Astrophysics Data System and by the JSTOR Archive.

APPENDIX A: EFFECT OF THE DENSITY THRESHOLD ON THE CLUMPING FACTOR

The density threshold used in simulations strongly affects the clumpiness of the gas, preventing reliable estimates of the recombination times.
In Figure A1 we compare, for the different simulations, the global clumping factors, C, defined as

$$C \equiv \frac{\sum_i m_i \rho_i^{-1} \sum_j m_j \rho_j}{\left(\sum_k m_k\right)^2} \qquad \text{(A1)}$$

where the indices i, j and k run over the total number of gas particles. At high z, the clumping factor remains quite flat with $C \sim 1$ until $z \sim 30 - 20$, for the mean density simulations, and $z \sim 70 - 60$, for the high density region. Afterward, there is a steep increment due to gas cooling and subsequent condensation.
As expected, the low threshold models underestimate C. The difference is as high as some orders of magnitude: in the low threshold simulations C is only $\sim 10 - 20$ at $z \simeq 10$, but in the high threshold ones, we get $C \sim 10^3$ at the same redshift.
The clumpiness of the high density region is $C(z \simeq 33) \sim 200$ and $C(z \simeq 31) \sim 10^3$.
The difference in clumping factors is caused by the fact that in the

low density threshold model high density gas particles are turned into stars and then removed by the winds relatively early, while in the high density threshold case they are allowed to reach values which are about three orders of magnitude larger.

REFERENCES

Abel T., Anninos P., Zhang Y., Norman M. L., 1997, New Astronomy, 2, 181
Abel T., Bryan G. L., Norman M. L., 2000, ApJ, 540, 39
Abel T., Bryan G. L., Norman M. L., 2002, Science, 295, 93
Brax P. H., Martin J., 1999, Physics Letters B, 468, 40
Bromm V., Larson R. B., 2004, ARA&A, 42, 79
Cen R., Ostriker J. P., 1992, ApJ, 399, L113
Ciardi B., Ferrara A., 2005, Space Science Reviews, 116, 625
Crociani D., Viel M., Moscardini L., Bartelmann M., Meneghetti M., 2008, MNRAS, 385, 728
Einstein A., 1917, Sitzungsberichte der Königlich Preußischen Akademie der Wissenschaften (Berlin), pp 142–152
Evrard A. E., 1988, MNRAS, 235, 911
Galli D., Palla F., 1998, A&A, 335, 403
Gao L., Yoshida N., Abel T., Frenk C. S., Jenkins A., Springel V., 2007, MNRAS, 378, 449
Gunn J. E., Gott J. R. I., 1972, ApJ, 176, 1
Haiman Z., Bryan G. L., 2006, ApJ, 650, 7
Hinshaw G., Weiland J. L., Hill R. S., 18 co-authors 2008, ArXiv e-prints, 803
Hollenbach D., McKee C. F., 1979, ApJS, 41, 555
Jeans J. H., 1902, Phil. Trans., 199, A p.1+
Jenkins A., Frenk C. S., White S. D. M., Colberg J. M., Cole S., Evrard A. E., Couchman H. M. P., Yoshida N., 2001, MNRAS, 321, 372
Katz N., Weinberg D. H., Hernquist L., 1996, ApJS, 105, 19
Maio U., Ciardi B., Dolag K., Tornatore L., 2008, in O'Shea B. W., Heger A., eds, First Stars III Vol. 990 of American Institute of Physics Conference Series, Cooling in Primordial Structure Formation. pp 33–35
Maio U., Dolag K., Ciardi B., Tornatore L., 2007, MNRAS, 379, 963
Maio U., Dolag K., Meneghetti M., Moscardini L., Yoshida N., Baccigalupi C., Bartelmann M., Perrotta F., 2006, MNRAS, 373, 869
Omukai K., Palla F., 2003, ApJ, 589, 677
Pawlik A. H., Schaye J., van Scherpenzeel E., 2008, ArXiv e-prints, 807
Peebles P. J., Ratra B., 2003, Reviews of Modern Physics, 75, 559
Peebles P. J. E., 1974, ApJ, 189, L51+
Peebles P. J. E., Dicke R. H., 1968, ApJ, 154, 891
Press W. H., Schechter P., 1974, ApJ, 187, 425
Ratra B., Peebles P. J. E., 1988, Phys. Rev. D, 37, 3406
Ricotti M., Gnedin N. Y., Shull J. M., 2002a, ApJ, 575, 33
Ricotti M., Gnedin N. Y., Shull J. M., 2002b, ApJ, 575, 49
Ricotti M., Gnedin N. Y., Shull J. M., 2008, ArXiv e-prints, 802
Saitoh T. R., Daisaka H., Kokubo E., Makino J., Okamoto T., Tomisaka K., Wada K., Yoshida N., 2008, ArXiv e-prints, 802
Saslaw W. C., Zipoy D., 1967, Nature, 216, 976
Sheth R. K., Tormen G., 1999, MNRAS, 308, 119
Springel V., 2005, MNRAS, 364, 1105
Springel V., Hernquist L., 2003, MNRAS, 339, 289
Tegmark M., Silk J., Rees M. J., Blanchard A., Abel T., Palla F., 1997, ApJ, 474, 1
Tornatore L., Borgani S., Dolag K., Matteucci F., 2007, MNRAS, 382, 1050
Tornatore L., Ferrara A., Schneider R., 2007, MNRAS, 382, 945
Whalen D., O'Shea B. W., Smidt J., Norman M. L., 2008, ApJ, 679, 925
Yoshida N., Abel T., Hernquist L., Sugiyama N., 2003, ApJ, 592, 645
Yoshida N., Omukai K., Hernquist L., 2007, ApJ, 667, L117
Yoshida N., Omukai K., Hernquist L., Abel T., 2006, ApJ, 652, 6